TOWARD ESTABLISHING A COMPREHENSIVE PRESSURE-SINKAGE MODEL FOR SMALL DIAMETER WHEELS ON DEFORMABLE TERRAINS

Gareth Meirion-Griffith and Matthew Spenko

Mechanical, Materials and Aerospace Engineering Department, Illinois Institute of Technology, Chicago, IL, 60616, USA

gmeirion@iit.edu, mspenko@iit.edu

Abstract

Traditional terramechanics theorems utilise pressure-sinkage models based on the assumption that the contact area between a tyre and soil can be approximated as a flat plate. Examples include work by Bekker, Reece, and Ishigami. Recently, the authors have demonstrated that 1) this approximation does not hold for wheels with a diameter less than approximately 50 cm and 2) an improved diameter-dependent pressure-sinkage model can yield more accurate results. In this paper, further improvements to the pressure-sinkage model for small diameter wheels are presented. First the diameter-dependent pressure-sinkage model is augmented with a geometric relationship to account for the normal stress distribution at the wheel-soil interface. Second, the effect of wheel width is investigated. The models are verified with field tests using a man-portable unmanned ground vehicle on wet sand and laboratory experiments on dilative (dry quartz sand) and compactive (kaolin-clay/silt mix) soils. Results indicate that the diameter-dependent pressure-sinkage model outperforms previous models in predicting drawbar pull as a function of slip and that the effect of wheel width on the pressure-sinkage model is highly dependent on the soil type.

Keywords: Pressure-sinkage, sinkage, wheel diameter, wheel width

1 Introduction

Pressure-sinkage models play a fundamental role in terramechanics. They are used to derive sinkage and resistance formulae, which are in turn used to derive performance metrics such as thrust and drawbar pull. The majority of pressure-sinkage models are based on the assumption that the contact area between a wheel and soil can be approximated as a flat plate [1, 2, 5, 6]. However, the authors have previously shown that this approximation is not valid for wheel diameters less than approximately 50 cm and developed a diameter-dependent pressure-sinkage model to account for this discrepancy [7]. This paper builds upon that work by 1) augmenting the diameter-dependent pressure-sinkage model with a geometric relationship to describe the shape of the normal stress distribution at the wheel-soil interface and 2) investigating the effect of wheel width.

Results from both field and laboratory experiments are presented. The results indicate that the diameter-dependent pressure-sinkage model exceeds previous models in predicting drawbar pull as a function of slip and that the effect of wheel width on the pressure-sinkage model is highly dependent on the soil type.

This paper is organized as follows. Section 2 provides a brief background into some of the most common pressure-sinkage models used in terramechanics. Section 3 discusses the augmentation of the aforementioned diam-

eter-dependent pressure-sinkage model with the geometric representation of normal stress. Section 4 details the application of this improved model in a numerical simulation used to predict vehicle tractive performance. The simulation results are compared to field tests performed using a 40 kg unmanned ground vehicle on sandy terrain. Last, section 5 discusses the results of an investigation into the effect of wheel width on the diameter-dependent model, which has previously been shown to be an important factor [2, 5, 9, 10].

2 Background

An introduction to the most prevalent pressure-sinkage models is presented here. Note that each of these models assumes that the normal pressure at the wheel-soil interface is equal to that for a rectangular, flat plate. This assumption is based on a large wheel undergoing a relatively small amount of sinkage.

The baseline pressure-sinkage model used in terramechanics is the Bernstein-Goriatchkin model [1]:

$$\sigma = kz^n \tag{1}$$

where σ is the normal pressure, k is the sinkage modulus, z is the sinkage, and n is the sinkage exponent. This model was developed by noting that the pressure-sinkage relationship for a flat plate fit the form of a power function. As such, k and n are curve fitting constants that fit experimentally observed data for a particular soil.

Bekker modified Eq. 1 by separating k into k_c (cohesive) and k_ϕ (frictional) moduli [2]:

$$\sigma = \left(\frac{k_c}{b} + k_\phi \right) z^n \tag{2}$$

where b is the width of the rectangular plate used to deform the soil. Note that for a frictional soil such as dry sand, k_c will be negligible. Similarly, for a highly cohesive soil such as wet clay, k_ϕ will have minimal effect.

Reece noted that the linear relationship between k_c and b implied by Bekker's model could be improved upon [5] by considering previous bearing capacity research [3, 4]. Reece found that the normal pressure beneath a rectangular plate could be given as [5]:

$$\sigma = \left[ck_c' + \gamma b k_\phi' \right] \left(\frac{z}{b} \right)^n \tag{3}$$

where k_c' and k_ϕ' are dimensionless constants and γ is the unit weight of the soil. He noted that although his model varied from Bekker's only its response to plate width, b, this was sufficient to mark a significant improvement.

In 2008, Ishigami modified Reece's equation to represent the two-dimensional, semi-elliptical distribution of normal stress at the wheel-soil interface [6]:

$$\sigma(\theta) = \left[ck_c' + \gamma b k_\phi' \right] \left(\frac{r}{b} \right)^n \left(\cos\theta - \cos\theta_s \right)^n \tag{4}$$

where θ is an arbitrary angle along the wheel-soil contact arc and θ_s is the static wheel-soil contact angle (see Fig. 1).

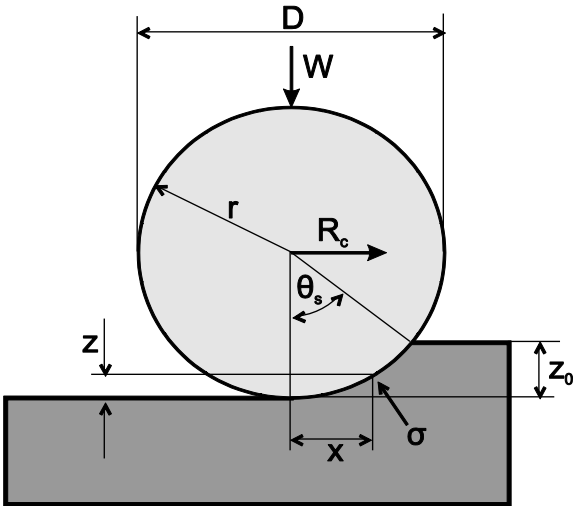

Fig. 1: *Wheel pressure sinkage geometry*

These relationships have shown to be accurate for a large wheel experiencing modest sinkage; however, as wheel diameter decreases, the curvature of the wheel-soil contact patch increases and the flat plate approximation loses validity. In 2010, the authors proposed a diameter dependent pressure-sinkage model, which has been shown to yield significantly improved accuracy for small diameter wheels [7]:

$$\sigma = \hat{k} z^{\hat{n}} D^{\hat{m}} \tag{5}$$

Here, $\hat{k}$, $\hat{n}$, and $\hat{m}$ are soil properties, which are derived in a manner similar to that proposed by Wong [8]. Further details on the derivation are available in [7].

This modified pressure-sinkage model enabled the derivation of modified wheel sinkage and compaction resistance equations. Again, these modified equations were shown to be more accurate than traditional terramechanics models for small, rigid wheels [7]. Wheel sinkage was derived as:

$$z_0 = \frac{3W}{b(3-\hat{n})\hat{k}D^{\hat{m}+0.5}}^{2/2\hat{n}+1} \quad (6)$$

where W is the normal load. Compaction resistance was derived as:

$$R_c = b\hat{k}D^{\hat{m}} \frac{z_0^{\hat{n}+1}}{\hat{n}+1} \quad (7)$$

3 Distribution of Normal Stress

The modified pressure-sinkage relationship presented in [7] did not take into account the semi-elliptical distribution of normal stress that exists beneath a wheel (see Fig. 2).

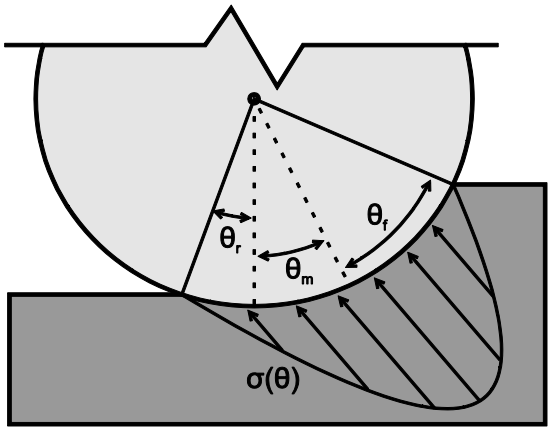

Fig. 2: *Normal stress distribution beneath a wheel*

To account for this distribution, Eq. 5 has been modified:

$$\sigma(\theta) = \hat{k}r^{\hat{n}}(\cos\theta - \cos\theta_s)^{\hat{n}} D^{\hat{m}} \quad (8)$$

where r is the wheel radius. This is the same approach Ishigami took in modifying Reece's equation. Using this pressure-sinkage model and re-derived sinkage and compaction resistance equations, a modified terramechanics framework has been established. This section details the application of this framework into a numerical simulation (see Fig. 3) that estimates the tractive performance of a wheeled vehicle. The methodology was first proposed by Wong and Reece [11] and more recently implemented by Ishigami [6] and Hutangkabodee [12]. The vehicle's configuration and soil parameters are used to estimate the distribution of normal and shear stresses at the wheel-soil interface. Thus, the forces acting on a vehicle and the vehicle's subsequent mobility performance can be determined.

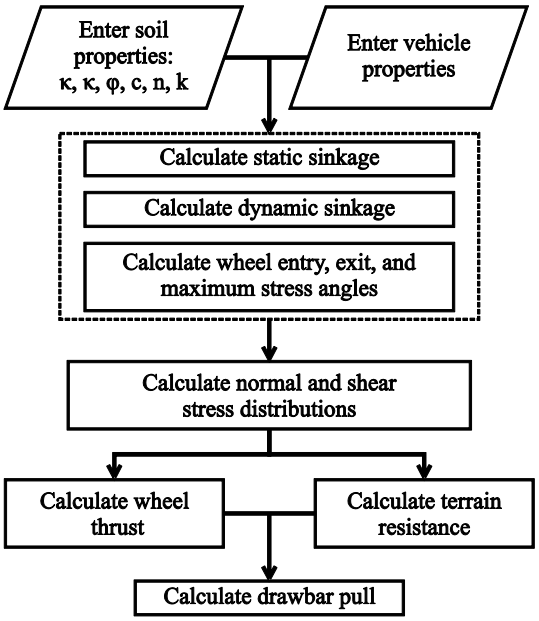

Fig. 3: *Schematic of numercial simulation*

Static sinkage can be determined using Eq. 6. Dynamic sinkage (slip sinkage) is the wheel sinkage incurred due to rutting at positive slip values and for a grouser-less tyre may be calculated using [13]:

$$z_d = K_{ss} z_0 \quad (9)$$

where:

$$K_{ss} = \frac{1+i}{1-0.5i} \quad (10)$$

and i is the wheel slip, given as:

$$i = \frac{\omega r - v_b}{\omega r} \quad (11)$$

where ω is the wheel angular velocity and v_b

is the vehicle body velocity.

Summing z_0 and z_d yields the total wheel sinkage, z_t, which is used to calculate the forward and rear wheel-soil contact angles, θ_f and θ_r, estimate the angle θ_m at which the maximum normal pressure occurs, and determine the shape of the normal stress distribution shown in Fig. 2. The normal stress as a function of θ is given as:

$$\sigma(\theta) = \hat{k} r^{\hat{n}} (\cos\theta - \cos\theta_s)^{\hat{n}} D^{\hat{m}} \qquad (12)$$

for $\theta_m \le \theta \le \theta_f$, and

$$\sigma(\theta) = \hat{k} r^{\hat{n}} \left[\cos\left\{ \theta_f - \frac{\theta - \theta_r}{\theta_m - \theta_r} (\theta_f - \theta_m) \right\} - \cos\theta_f \right]^{\hat{n}} D^{\hat{m}}$$

for $\theta_r \le \theta \le \theta_m$.

The angular location of maximum normal stress, θ_m, may be approximated as [14]:

$$\theta_m = \frac{\theta_r + \theta_f}{2} \qquad (13)$$

Longitudinal shear stress, used for forward locomotion, may be calculated using the Janosi-Hanamoto equation [15]:

$$\tau = \tau_{\max} \left(1 - \exp^{-j/\kappa}\right) \qquad (14)$$

where τ_{max} is the soil shear strength, κ is the shear deformation modulus, and j is the longitudinal soil deformation:

$$j(\theta) = r\left[\theta_f - \theta - (1-i)(\sin\theta_f - \sin\theta)\right] \qquad (15)$$

The shear and normal stresses may be combined to give an estimate of the total stress/force acting on a wheel and thus the drawbar pull, given as:

$$DP = rb \int_{\theta_r}^{\theta_f} \{\tau(\theta)\cos\theta - \sigma(\theta)\sin\theta\} d\theta \qquad (16)$$

The above equations were simulated numerically to predict vehicle tractive performance. The result is a prediction of drawbar pull, *DP*, as a function of wheel slip. The relationship provides insight into the total traction and efficiency of a vehicle. The simulation may be configured to use any of the aforementioned pressure-sinkage models. Simulated results are compared in the following section with those obtained in the field using an experimental unmanned ground vehicle.

4 Field Test Results

Field tests were performed in an outdoor testing facility on wet sand to validate the theoretical approach described in Section 3. The geotechnical properties of the sand are given in Table 1.

Table 1: Field test sand properties

Parameter	**Value**	**Units**
z modulus, $\hat{k}$	212.58	$kN/m^{\hat{n}+\hat{m}+2}$
Cohesion, c	3.0	*kPa*
Friction angle, ϕ	27.0	*deg*
Shear modulus, κ	0.025	*m*
z exponent, $\hat{n}$	0.82	*N/A*
D exponent, $\hat{m}$	-0.364	*N/A*

Tests were performed using the IIT Robotics Laboratory's *Variable Inertia Vehicle* (VIV) (see Fig. 4) [16].

Fig. 4: *Variable Inertial Vehicle*

The VIV is a 40 kg, rear-wheel drive, front wheel Ackermann steered unmanned ground vehicle. It is equipped with Qing DA, smooth-tread tyres (20 cm diameter, 8 cm width). The tyres are inflated to 20 psi and are stiff enough to be considered rigid. The VIV possesses two 250 W drive motors that can provide 1.9 Nm of constant torque and 8.5 Nm of peak torque. The vehicle has a maximum speed of 10 m/s. It also has the unique capability to change its centre of mass location. For the tests discussed here, this capability is used to evaluate how static load distribution affects vehicle tractive performance.

The VIV was accelerated by applying an 8.5 Nm torque to each of the rear wheels.

Acceleration was measured with a Novatel Span/CPT inertial navigation system and used to calculate the generated traction. The shifting mass was placed at three locations: forward, mid, and rear to ascertain the effect of mass distribution on the vehicle's performance. These positions correspond to a front/rear mass distribution of 71/29%, 50/50%, and 32/68%, respectively.

Results show the tractive performance of the VIV accelerating in a straight line (see Figs. 5, 6 and 7). Experimental results are represented by dots. The dashed and square markers represent the simulated Bekker and Reece models, respectively. The solid lines represent simulated data using the diameter-dependent model.

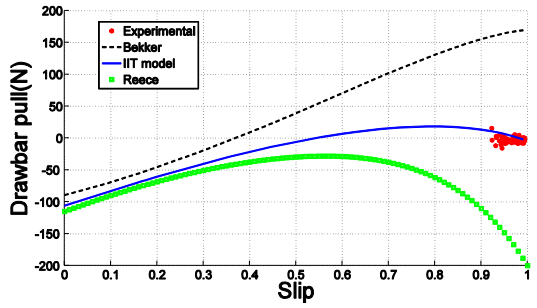

Fig. 5: *Drawbar pull versus slip with the shifting mass at the front of the VIV*

When the shifting mass is located at the front (Fig. 5), it is clear that the vehicle undergoes a high level of slip. This is due to an increase in the forward normal loading which causes increased sinkage. The slip results in further dynamic sinkage of the rear wheels due to rutting as the vehicle struggles to generate traction. This leads to greatly increased soil resistance, culminating in the vehicle's immobilisation. This is exemplified by the low drawbar pull values. The experimental data shows good agreement with the modified terramechanics framework, whereas Bekker's model is shown to overestimate the vehicle's performance. This is problematic. If a vehicle's mobility system were designed based Bekker's equations, it may exhibit lower performance in the field than expected. This could lead to increased mission time and cost or even immobilisation. Reece's model underestimates the vehicle's performance, especially at high slip levels.

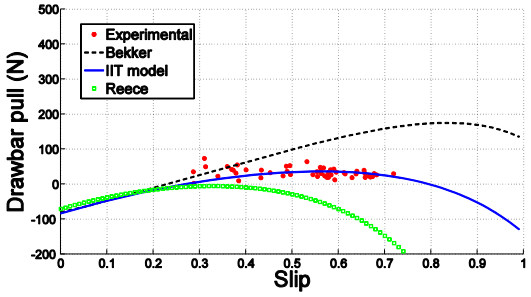

Fig. 6: *Drawbar pull versus slip with the shifting mass at the centre of the VIV*

In the case of the centred shifting mass the tractive performance is increased substantially and a mean acceleration of 0.75 m/s^2 was observed. For comparison, the VIV can accelerate at 3 m/s^2 on rigid terrain. A good agreement between experimental and simulated results using the modified equations is shown. Again, Bekker's model overestimates while Reece's model underestimates performance.

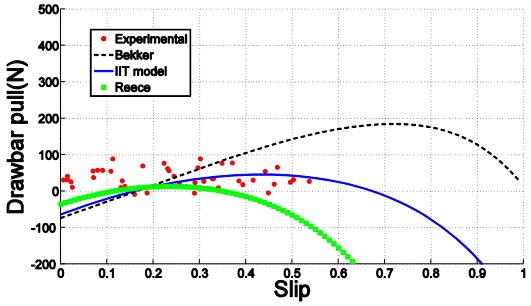

Fig. 7: *Drawbar pull versus slip with the shifting mass at the rear of the VIV*

An average acceleration of 1.1 m/s^2 was observed when the shifting mass was at the rear (see Fig. 7). Wheel slip was substantially reduced, averaging around 30%. This implies that the vehicle able to both generate more traction and do it more efficiently. However, the field test data has a wide spread. This may be caused by varying terrain properties or irregularities. In this configuration, the vehicle may also have experienced a wider range of DP/slip ratios due to its quick acceleration. As in the previous two experiments, the experimental data shows a better agreement with the modified terramechanics framework than Bekker's or Reece's models. However, it is

premature to draw conclusions from this experiment due to the spread of data.

In summary, the field tests demonstrate that the modified terramechanics framework presented here shows good agreement with experimental data taken for a small-wheeled UGV.

5 Width Dependence of the Pressure-Sinkage Model

As stated in Section 2, the modified pressure-sinkage model, Eq. 5, proposed by the authors in 2010 is independent of wheel width, *b*. Multiple authors have shown width to be an important factor in pressure-sinkage modelling [2, 5, 9, 10]. This section extends the work presented in Sections 2 and 3 to detail the results of an investigation into the effect of wheel width on (5). Experiments were performed using the pressure-sinkage testbed shown in Fig. 8:

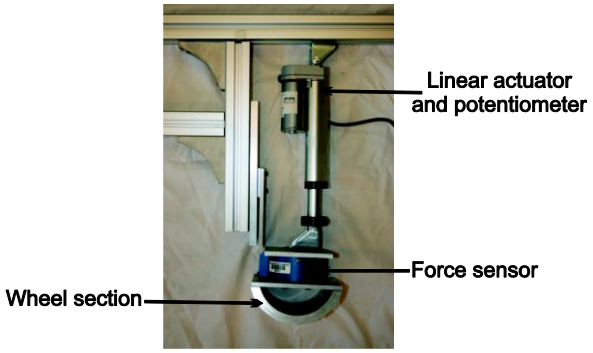

Fig. 8: *Pressure-sinkage testbed*

Over one hundred and twenty pressure-sinkage tests were carried out as part of this investigation. Fifteen wheel sections were tested, ranging from 13 mm to 203 mm in width and 114 mm to 265 mm in diameter. These dimensions were chosen to represent wheels used on modern UGVs [17, 18, 19]. Normal loads of up to 450 N were applied during testing. Normal load and sinkage were measured using a JR3 six-axis force-torque sensor and linear potentiometer. Two soils were used during testing: a Kaolin clay/silt mix (80% clay by volume) and dry quartz sand. These soils were chosen to represent compactive and dilative soils, respectively. The geotechnical properties of these soils are given in Tables 2 and 3.

Table 2: Geotechnical properties of clay/silt mix

Parameter	**Value**	**Units**
z modulus, $\hat{k}$	11.7	$kN/m^{\hat{n}+\hat{m}+2}$
Cohesion, c	10.6	*kPa*
Friction angle, ϕ	10.1	*deg*
z exponent, $\hat{n}$	0.77	*N/A*
D exponent, $\hat{m}$	-0.371	*N/A*

Table 3: Geotechnical properties of dry quartz sand

Parameter	**Value**	**Units**
z modulus, $\hat{k}$	1604	$kN/m^{\hat{n}+\hat{m}+2}$
Cohesion, c	2.05	*kPa*
Friction angle, ϕ	27.5	*deg*
z exponent, $\hat{n}$	0.8	*N/A*
D exponent, $\hat{m}$	0.39	*N/A*

5.1 Discussion of Clay/Silt Mix Results

The experimental results for the clay/silt mix are shown in Figs. 9, 10 and 11. Figure 9 represents five different wheel widths at a constant diameter of 114 mm. Figures 10 and 11 display similar results for wheel diameters of 178 mm and 267 mm, respectively. Note that the results for widths of 102 mm and 203 mm overlap in all three figures.

Several observations can be made. First, the pressure-sinkage relationship for the clay/silt mix exhibits a clear dependence on wheel width. Second, this dependence shows a decrease in pressure as wheel width increases. This is the same effect observed in [7] for an increase in wheel diameter. This implies that an increase in wheel-soil contact area, whether by a diameter or width change, yields a similar response to the pressure-sinkage curve. Third, the dependence on wheel width is conserved across all three diameters tested. Fourth, the curvature of the power functions changes as a function of wheel diameter in a manner conducive to the findings made in [7]. Last, the width dependence decays as width is increased. This can be seen in Figs. 9, 10 and 11 where the pressure-sinkage curves for widths of 102 mm and 203 mm overlap. It is

reasonable to suggest that at low widths the edge effects of the wheel-soil indentation are large, whereas for a large wheel width, the effects may be negligible. This would explain the similarity in results between larger wheel widths.

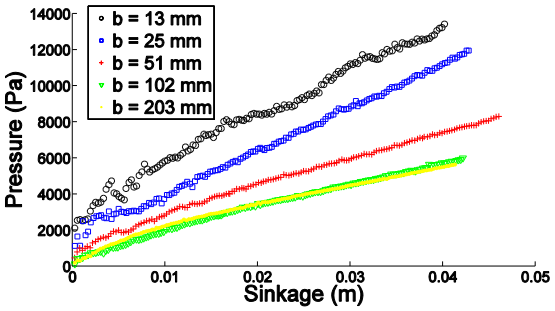

Fig. 9: *Width dependence for a 114 mm diameter wheel on a clay/silt mix*

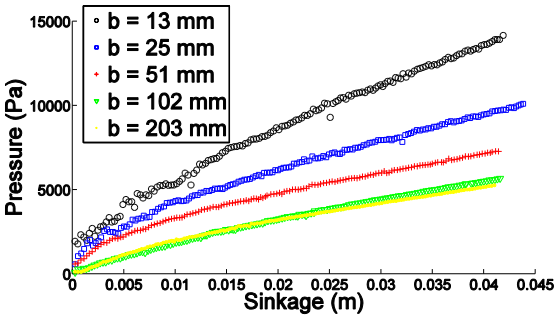

Fig. 10: *Width dependence for a 178 mm diameter wheel on a clay/silt mix*

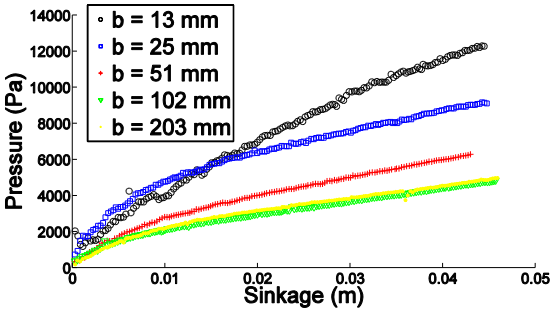

Fig. 11: *Width dependence for a 267 mm diameter wheel on a clay/silt mix*

5.2 A Comprehensive Pressure-Sinkage Model for Compactive Soils

Having reviewed the trends and characteristics of the pressure-sinkage curves for various wheel widths, a comprehensive model for compactive soils is proposed here. Given the independence of the effects of D and b and the similarity in their influence on the curve curvature (both cause a reduction in pressure as their dimensions increase), it was found that for compactive soils normal pressure may be expressed as:

$$\sigma(\theta) = \hat{k} r^{\hat{n}} (\cos\theta - \cos\theta_s)^{\hat{n}} (bl)^{\hat{m}} \quad (17)$$

where l is the projected length of the wheel-soil contact patch, given by:

$$l = \sqrt{\left(\frac{D}{2}\right)^2 - \left(\frac{D}{2} - z_0\right)^2} \quad (18)$$

The form of Eq. 17 allows the pressure at the wheel-soil interface to be a function of both b and D. Although the accuracy of Eq. 17 for the experimental results presented here was found to be good ($R^2 = 0.96$), tests on more compactive soils should be performed to further validate the model.

As shall be seen in Section 4.3, this relationship does not hold for the dilative sand, where the effects of b and D on the pressure-sinkage relationship appear to be coupled.

5.3 Discussion of Dry Quartz Sand Results

The experimental width dependence results for the dry quartz sand are shown in Figs. 12, 13 and 14.

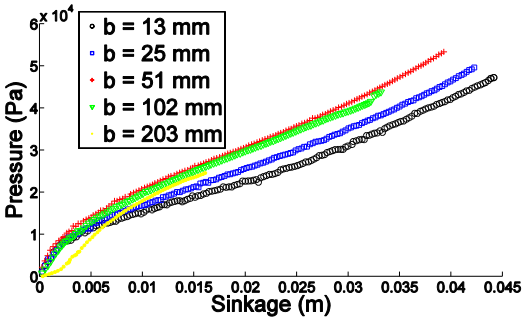

Fig. 12: *Width dependence for a 114 mm diameter wheel on dry quartz sand*

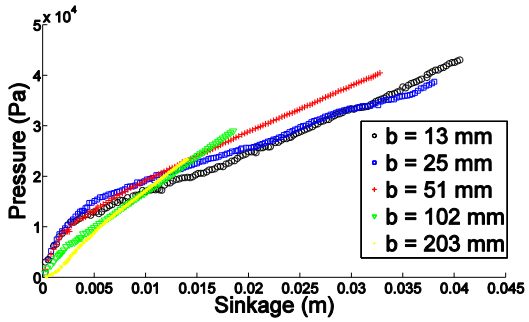

Fig. 13: *Width dependence for a 178 mm diameter wheel on dry quartz sand*

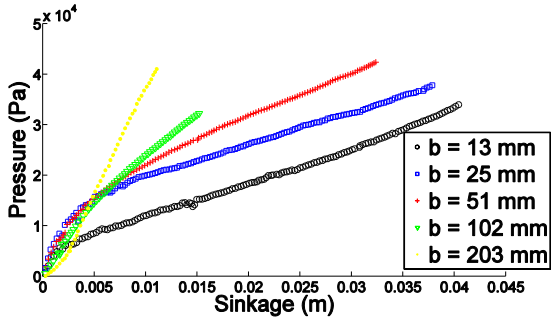

Fig. 14: *Width dependence for a 267 mm diameter wheel on dry quartz sand*

It is clear that the width dependence of this soil is more complex than that of the compactive clay/silt mix. For the 114 mm diameter wheel, there appears to be no discernable width dependence. Similarly for the 178 mm diameter wheel, little dependence on wheel width is displayed. It could be argued, however, that the gradient of the curves generally increases with wheel width. This trend is particularly apparent for the 267 mm diameter wheel. For this wheel diameter, an increase in wheel width yields an increase in pressure.

Reviewing each figure, it appears that the effect of wheel width on the pressure-sinkage relationship grows proportionally to wheel diameter. That is, as wheel diameter increases, so does the effect of wheel width.

For the dry sand, the effects of wheel width and diameter on the pressure-sinkage relationship appear to be coupled. This is in contrast to the results found for the compactive soil. It seems likely that there is a relationship between D and b, such that when one is geometrically dominant, the effect of the other dimension is reduced. At this stage of the investigation, however, this conclusion is speculative. Further tests must be performed using a wider range of both wheel diameters and widths to determine an accurate model for dilative soils.

6 Conclusion

This paper developed a more accurate pressure-sinkage model for small diameter wheels by including the effects of the semi-elliptical distribution of normal stress beneath a wheel. Experimental results indicate that the proposed model offers better predictive capabilities on wet sand than previous pressure-sinkage models. Additionally, the effect of width on the pressure-sinkage model has been investigated. Of particular interest is the difference in soil response between compactive and dilative soils. Further experimentation and theoretical development is required before a comprehensive pressure-sinkage model can be produced for both soil types.

Nomenclature

b	Wheel width	*[m]*
c	Soil cohesion	*[Pa]*
D	Wheel diameter	*[m]*
i	Wheel slip	*[-]*
j	Longitudinal soil deformation	*[m]*
k	Bernstein sinkage mod.	kN/m^{n+2}
$\hat{k}$	Griffith-Spenko sinkage mod.	$kN/m^{\hat{n}+\hat{m}+2}$
k_c	Bekker cohesive sinkage mod.	kN/m^{n+1}
k_ϕ	Bekker frictional sinkage mod.	kN/m^{n+2}
k'_c	Reece cohesive sinkage mod.	*[-]*
k'_ϕ	Reece frictional sinkage mod.	*[-]*
$\hat{m}$	Griffith-Spenko diameter exponent	*[-]*
n	Bernstein sinkage exponent	*[-]*
$\hat{n}$	Griffith-Spenko sinkage exponent	*[-]*
r	Wheel radius	*[m]*
R_c	Compaction resistance	*[N]*
W	Weight	*[N]*
z	Sinkage at max normal stress	*[m]*
z_0	Static sinkage	*[m]*
z_d	Dynamic sinkage	*[m]*
γ	Soil unit weight	$[N/m^3]$
κ	Shear deformation mod.	*[m]*
θ	Arbitrary wheel arc angle	*[rad]*
θ_f	Forward wheel-soil contact angle	*[rad]*

θ_r	Rear wheel-soil contact angle	*[rad]*
θ_s	Static wheel-soil contact angle	*[rad]*
σ	Normal stress	*[Pa]*
τ	Shear stress	*[Pa]*
ω	Wheel angular velocity	*[rad/s]*

References

[1] Bernstein, R. Probleme zur Experimentellen Motorpflugmechanik. Der Motorwagen, 16, 1913.

[2] Bekker, M. G. Theory of Land Locomotion, vol. I. University of Michigan Press, Ann Arbor, MI, USA, 1962.

[3] Meyerhoff, G. G. The Ultimate Bearing Capacity of Foundations. Geotechnique, Vol. 2, 1951.

[4] Terzaghi, K. Theoretical Soil Mechanics, J. Wiley & Sons, New York, USA, 1944.

[5] Reece, A. Principles of Soil-Vehicle Mechanics. Institution of Mechanical Engineers, 180, U.K., 1964.

[6] Ishigami, G. Terramechanics-Based Analysis and Control for Lunar/Planetary Exploration Robots. Ph.D. thesis, Tohoku University, Tohoku, Japan, 2008.

[7] Meirion-Griffith, G. and Spenko, M. A Modified Pressure-Sinkage Model for Small, Rigid Wheels on Deformable Terrains. Journal of Terramechanics, 48(2), 149-155, 2011.

[8] Wong, J. Y. Theory of Ground Vehicles, vol. IV. John Wiley & Sons, Ottawa, Canada, 2008.

[9] Upadhyaya, S. and Wulfsohn, D. and Mehlschau, J. An Instrumented Device to Obtain Traction Related Parameters, Journal of Terramechanics (30), 1993.

[10] Lyasko, M. LSA Model for Sinkage Predictions. Journal of Terramechanics, 47: 1 – 19, 2010.

[11] Wong, J. Y. and Reece, A. R. Prediction of Rigid Wheel Performance Based on the Analysis of Soil-Wheel Stresses. Journal of Terramechanics, 4, 1967.

[12] Hutangkabodee, S. Soil Parameter Identification for Wheel-Terrain Interaction Dynamics and Traversability Prediction. International Journal of Automation and Computing, 3:244-251, 2006.

[13] Lyasko, M. Slip Sinkage Effect in Soil-Vehicle Mechanics. Journal of Terramechanics, 47:21-31, 2010.

[14] Iagnemma, K. Online Terrain Parameter Estimation for Wheeled Mobile Robots with Application to Planetary Rovers. IEEE Transactions on Robotics, 20:921-927, 2004.

[15] Janosi, Z. and Hanamoto, B. An Analytical Determination of Drawbar Pull as a Function of Slip for Tracked Vehicles in Deformable Soils, 1st International Conference on the Mechanics of Soil-Vehicle Systems, Turin, Italy, 1961.

[16] Nie, C. and Spenko, M. Design and Experimental Validation of an Unmanned Ground Vehicle with Variable Inertial Properties, IROS Conference, CA, USA, 2011 (to appear).

[17] Lindemann, R. and Vorhees, C. Mars Exploration Rover Mobility Assembly Design, Test and Performance, IEEE SMC Conference, HI, USA, 2005.

[18] Yu, H., Spenko, M. and Dubowski, S. Omnidirectional Mobility Using Active Split Offset Castors, ASME Journal of Mechanical Design, Vol. 126:822-829, 2004.

[19] Pederson, L. and Aposolopoulos, D. Rover Design For Polar Astrobiological Exploration, NASA Ames Research Center, 2005.